Journal of Volcanology and Geothermal Research 421 (2022) 107425

Contents lists available at ScienceDirect

Journal of Volcanology and Geothermal Research

journal homepage: www.elsevier.com/locate/jvolgeores

New insights on faulting and intrusion processes during the June 2007, East Rift Zone eruption of Kīlauea volcano, Hawai'i

J. Leeburn [a], C. Wauthier [a,b,*], E. Montgomery-Brown [c], J. Gonzalez-Santana [a]

[a] Department of Geosciences, The Pennsylvania State University, USA
[b] Institute for Computational and Data Sciences, ICDS, The Pennsylvania State University, USA
[c] California Volcano Observatory, USGS, USA

ARTICLE INFO

Article history:
Received 28 December 2020
Received in revised form 3 November 2021
Accepted 8 November 2021
Available online 12 November 2021

Keywords:
Natural hazard
Kīlauea
InSAR
East Rift Zone
Geodetic modeling
Coulomb stress changes

ABSTRACT

The East Rift Zone (ERZ) of Kīlauea Volcano, Hawai'i, represents one of the most volcanically active regions in the world. The 2007 Father's Day (FD) dike intrusion, eruption, and accompanying slow-slip event (SSE) has been previously modeled using geodetic data to constrain the geometry of the intrusion and the timing and magnitude of the SSE. Here, we perform inversions of three interferometric synthetic aperture radar (InSAR) datasets and a new intensity offset tracking dataset to assess the effect of integrating intensity cross-correlation offsets into inversion problems and explore additional potential models for the intrusion geometry of the FD event based on this additional data. The overall lowest misfit single Okada model for all datasets opens 2.3 m, strikes 73 degrees while dipping sub-vertically at 83 degrees, and extends approximately 2.9 km to the ENE and 2.4 km downdip. The differences are minor between complex en-echelon distributed Okada and decollement model of (Montgomery-Brown et al., 2010) or 3D-MBEM breaching models including multiple surface breaches and free-slipping decollement movement. Finally, we examine the static Coulomb stress changes for the proposed decollement fault created by our preferred model and a representative model of deep rift opening and find that deep rift zones dilation, not shallow ERZ intrusions, are likely modulating slip on the decollement.

1. Introduction

The rift zone eruptions of Kīlauea volcano, Hawaii, are part of a complex feedback relationship between magma movement throughout the volcano's plumbing system and fault-related stresses accommodated via slip along a basal decollement fault (Poland et al., 2014; Syracuse et al., 2010; Montgomery-Brown et al., 2010; Lundgren et al., 2013). Vents along the volcano's two primary rift zones (Fig. 1) are fed by diking events (Fig. 2) which deliver magma from conduits along the shallow rift zones to the surface (Poland et al., 2014). These diking events are chiefly driven by either high-pressure magma delivered directly from storage in summit reservoirs (active intrusions), or tensional stress fields created by local extension that encourages upward magma propagation (passive intrusions) (Conway et al., 2018; Poland et al., 2014). A long-term rift zone eruption spanned 1983 to 2018 (Heliker and Mattox, 2003) and included multiple episodes of active and passive intrusive activity which were examined by remote sensing and in-situ geodetic and geophysical techniques (Wright and Klein, 2014; Poland et al., 2014; Conway et al., 2018). The Father's Day (FD) intrusive event of June 17, 2007, has been classified as an active event, as uplift prior to the event and higher magma temperature relative to the eruptive intrusion of 1997 suggests an active pressurized intrusion of magma (Montgomery-Brown et al., 2010; Anderson and Poland, 2016), while geodetic models have indicated that concurrent slow-slip may have been triggered by the intrusion (Brooks et al., 2008; Montgomery-Brown et al., 2010). However, the possibility of stress changes introduced by slow slip of a decollement fault beneath the south flank has led other studies to classify the FD event as a hybrid intrusion, combining both active and passive effects (Poland et al., 2014).

Several previous studies have investigated the June 2007 FD event, with the most comprehensive including inversion sequences to test several candidate dike and decollement models based on InSAR, GPS, and tilt data (Montgomery-Brown et al., 2010). Others have investigated the slow slip behavior of the decollement during the 2007 FD event (Brooks, 2008; Syracuse et al., 2010; Montgomery-Brown et al., 2010, 2013) and Kīlauea's other rift zone intrusion events in 1983, 1993, 1999, and 2011 (Cayol et al., 2000; Owen et al., 2000; Cervelli et al., 2002; Lundgren et al., 2013; Montgomery-Brown et al., 2013; Conway et al., 2018) (Fig. 2), although only (Montgomery-Brown et al., 2010) and (Lundgren et al., 2013) include decollement slip during the

* Corresponding author at: Department of Geosciences, The Pennsylvania State University, USA.
E-mail address: cuw25@psu.edu (C. Wauthier).

https://doi.org/10.1016/j.jvolgeores.2021.107425

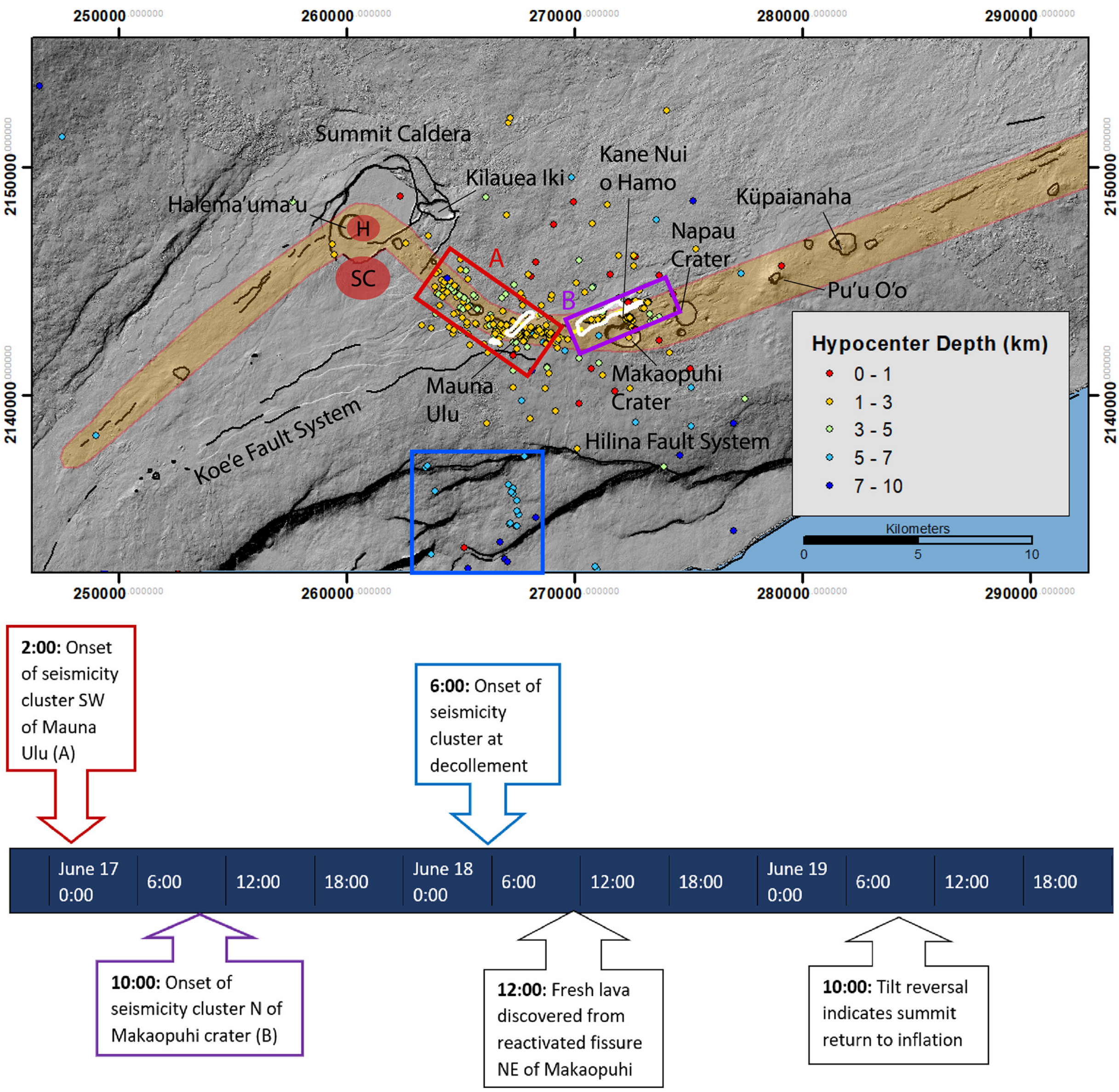

Fig. 1. Overview of seismicity hypocenters observed between 0:00 on June 17, 2007, and 23:59 on June 20, 2007 local time. Box colors correspond to timeline events as described in Section 2.2. White outlines indicate regions of cracked and steaming ground as observed by field observations conducted on June 20, 2007. Halema'uma'u and South Caldera reservoirs not to scale.

modeled intrusion for the 2007 and 2011 intrusion events, respectively. However, the feedback relationship between the intrusion and slow slip portions of both events remains unclear. We seek here to expand upon previous analysis by utilizing a guided Monte Carlo optimization inversion to further explore favorable models, employing both simple analytic solutions (Okada, 1985) and a more complex numerical 3D Mixed Boundary Element Method (3D-MBEM, Cayol and Cornet, 1997). The latter allows for the modeling of a uniform dike overpressure leading to realistic distributions of opening for intrusions under a physically plausible assumption of a hydraulic connection between all parts of a single intrusion. 3D-MBEM also allows any shape and number of mechanically interacting stress sources while considering potential connections with the ground surface through mapped eruptive fissures (Fukushima et al., 2005). To assess changes in model fit, we additionally employ a new dataset based on pixel offset correlation, allowing for the inclusion of near-field deformation which would otherwise be lost due to signal decorrelation of regular interferograms. Finally, we calculate Coulomb stress changes to explore the results of our optimal models, their implications for the intrusion geometry of the 2007 FD, and the nature of feedback relationships and potential triggering between Kīlauea's rift zone eruptions and decollement slip behavior.

2. Background

2.1. Geological history and evolution of Kīlauea

Two areas of magma storage characterize Kīlauea's magma reservoir system, with the larger primary source (South Caldera, “SC”, in Fig. 1) residing just south of Kīlauea's main caldera at an estimated depth between 2 and 5 km below the surface (Owen et al., 2000; Cervelli and Miklius, 2003; Wright and Klein, 2014; Poland et al., 2014; Neal et al., 2019). Although this reservoir has long been noted as the primary focus of continuing summit deformation, its exact geometry is poorly constrained with multiple candidate geometries fitting the data well (Pietruszka and Garcia, 1999; Cervelli and Miklius, 2003; Garcia, 2003; Baker and Amelung, 2012; Wauthier et al., 2016; Poland et al., 2014).

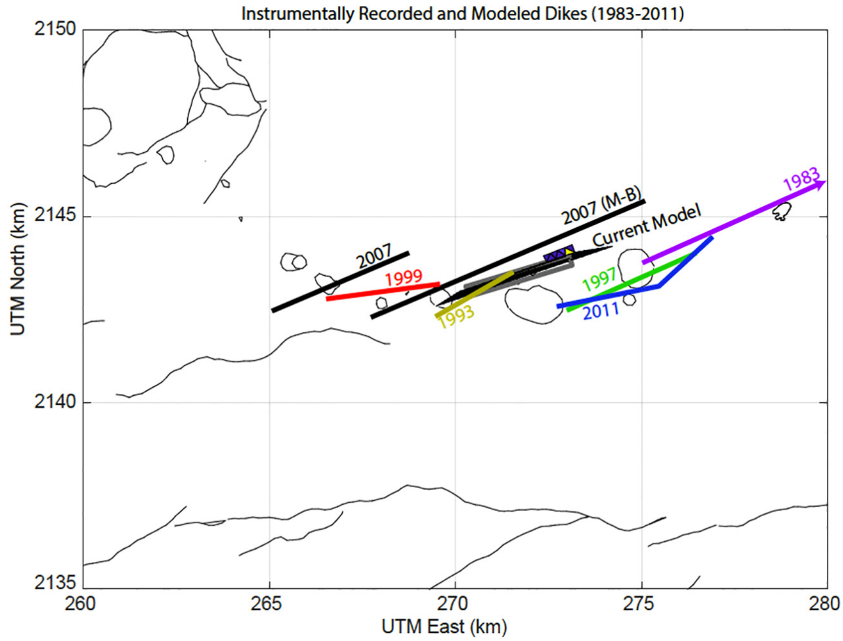

Fig. 2. Map view of modeled ERZ dike traces discussed this study and (Cervelli et al., 2002; Montgomery-Brown et al., 2010; Lundgren et al., 2013; Conway et al., 2018; Montgomery-Brown and Miklius, 2021). (For interpretation of the references to color in this figure legend, the reader is referred to the web version of this article.)

The second storage area (Halemaʻumaʻu, "H", in Fig. 1) exists slightly east of the pre-2018 collapse of Halemaʻumaʻu crater, and is both smaller and shallower than the SC summit reservoir at a depth of 1–2 km (Anderson et al., 2015; Bagnardi et al., 2014). The East Rift Zone (ERZ) and Southwest Rift Zone (SWRZ) are connected to these two source regions and curve away from the summit to the east and southwest, respectively (Fig. 1) (Macdonald et al., 1983). Historic eruptions of Kīlauea have generally occurred as either summit activity centered on Halemaʻumaʻu crater or eruptions issuing from vents along the two rift zones (Macdonald et al., 1983; Wright and Klein, 2014).

Eruptive events at Kīlauea are frequently accompanied by motion along a decollement fault which forms the interface between the volcano and the seafloor at approximately 6–10 km depth and allows the volcano's southern flank to slip southward toward the ocean (Hill, 1969; Hill and Zucca, 1987; Delaney et al., 1990; Denlinger and Okubo, 1995). This fault has been observed to accommodate several types of movement, including steady-state creep (Owen et al., 2000), sudden catastrophic rupture creating large earthquakes (e.g., Liu et al., 2018), and slow-slip events (SSEs) characterized by accelerated slip rate (15–20 cm over two days) and aftershock microseismicity (Brooks et al., 2006; Syracuse et al., 2010; Montgomery-Brown et al., 2013; Cervelli et al., 2002). The exact relationship between magma movement and fault motion remains elusive. Some studies suggest pressure-driven dilation (e.g., Denlinger and Okubo, 1995; Cayol et al., 2000; Conway et al., 2018) and/or dense cumulate formation in the deep ERZ below 3–4 km induces motion along the fault (Delaney et al., 1990; Poland et al., 2014). There likely exists a complicated feedback system wherein increasing magma pressure promotes fault movement, while decreasing least compressive stresses caused by fault slip encourage further magma transport throughout the ERZ conduit.

Beginning on January 3, 1983, Kīlauea entered a continuous eruptive sequence characterized by repeated diking events and lava fountaining, primarily from the vents Puʻu ʻŌʻō and Kūpaianaha along the ERZ (Heliker and Mattox, 2003; Wright and Klein, 2014). The formation of a persistent lava lake at the bottom of Halema'uma'u in March 2008, marked the first simultaneous instance of sustained rift and summit activity (Wright and Klein, 2014), with this lava lake persisting until the lower East Rift Zone (LERZ) intrusion and eruption of 2018 (Neal et al., 2019). On April 30 of 2018, sudden deflation of Puʻu ʻŌʻō and increased seismicity indicated magma movement down-rift of the vent. Fissures opened in the LERZ and continued erupting until August 4 in the most effusive sequences on modern record for Kīlauea (Lundgren et al., 2019). On May 4, the decollement fault slipped catastrophically, creating a moment magnitude 6.9 earthquake offshore, the largest observed since the 1975 M7.7 event (Liu et al., 2018). Kīlauea's summit caldera underwent episodic subsidence and collapse events between May 4 and August 42,018, eventually creating a void of ~0.825 km^3, roughly equivalent to the amount of magma erupted down-rift (Neal et al., 2019). This eruptive sequence evidently exhausted the summit magma supply sufficiently to return the system to a period of recharge and relative quiescence, ending the 35-year Puʻu ʻŌʻō eruption.

2.2. The 2007 Father's Day (FD) event

From 1983 until late 2003, the Puʻu ʻŌʻō-Kūpaianaha eruption dominantly exhibited deflationary deformation at Kīlauea's summit likely due to a steady flow of magma throughout the volcano's plumbing system which replaced stored magma with fresh, primitive material from the mantle source (Poland et al., 2014. Beginning in 2003, this summit deformation switched to inflation indicating an accumulation of magma in Kīlauea's two primary magma reservoirs. Sulfur dioxide emission rates increased slightly during this period, suggesting the inflation stemmed from an increase in the rate of supply directly from the mantle source instead of a blockage in the eruptive pathway (Poland et al., 2008, Poland et al., 2014). Gradual dilation of the upper SWRZ throughout 2006 and Coulomb stress calculations for summit-area seismicity indicated additional magma accumulation beyond the summit storage system, reinforcing the existing evidence for an increase in magma supply to the entire complex (Myer et al., 2008; Wauthier et al., 2016). On May 24, 2007, shortly before the FD event, a pair of magnitude 4+ earthquakes occurred along strike-slip faults beneath the upper ERZ further indicating pressurization of magma storage at the summit (Wauthier et al., 2013).

Early morning on June 17, 2007, deflation and heightened seismicity in the summit and upper ERZ along with the opening of cracks near Makaopuhi crater indicated magma intrusion beginning near Mauna Ulu and moving east (Fig. 1, cluster A, white outlines) (Global Volcanism Program [GVP], 2009). Deflation began at Puʻu ʻŌʻō shortly thereafter, dropping the floor of the crater a total of approximately 80 m by the end of the event and disrupting magma supply at the vent (Poland et al., 2008). By approximately 10:00 am local time, seismicity moved east to the north rim of Makaopuhi and a small volume of lava erupted from a short (~200 m) fissure which formed to the north east of Kane Nui o Hamo at the end of a second region of cracked and steaming ground (Fig. 1, cluster B, white outlines). The exact timing of this eruption is uncertain as the small lava flow was not discovered until the following day along with the regions of cracked ground (Tim Orr, Pers. Comm., 2020). The cluster A of seismicity and associated and cracking area (Fig. 1) might also be related to normal slip on a fault pertaining to the Koa'e fault zone as it was observed during the September 1999 ERZ intrusion (Cervelli et al., 2002) and other intrusive events (Swanson et al., 2018). A small discontinuity related to this motion was identified in InSAR displacements by Montgomery-Brown et al. (2010) and is also highlighted on Fig. 3.

Approximately 20 h after the initial onset of rift zone seismicity, additional earthquakes were detected clustering near 6.5–8 km depth at a location typically indicative of SSEs (Fig. 1) (Brooks, 2008; Syracuse et al., 2010). GPS stations located along the southern flank beyond the influence of the intrusion deformation field recorded uniform motion to the south and slightly east, confirming the presence of an independent SSE shortly following the intrusion (Brooks, 2008; Montgomery-Brown et al., 2010, 2013). By late day June 19, initial deflation observed near the summit and upper ERZ transitioned back to inflation as rift zone seismicity dropped to pre-event levels (Poland et al., 2008). A combination of GPS data showing cumulative extension of approximately 100 cm during the event in some locations along with substantial deflation at Puʻu ʻŌʻō indicates considerable draining of summit magma into storage along the ERZ (Global Volcanism Program [GVP], 2009).

Sulfur dioxide emissions at the summit declined substantially to approximately 200 tons per day at the summit, and Puʻu ʻŌʻō continued deflating until the resumption of eruptive activity on July 1 with the onset of a separate rift zone event at Puʻu ʻŌʻō (Poland et al., 2008). The next intrusive event occurred on July 21 as the short-term opening of an eruptive fissure between Puʻu ʻŌʻō and Kūpaianaha, with its eastern extent terminating in a new eruptive vent which would continue to exhibit lava effusion from July 21, 2007 to March 5, 2011 (Poland et al., 2014).

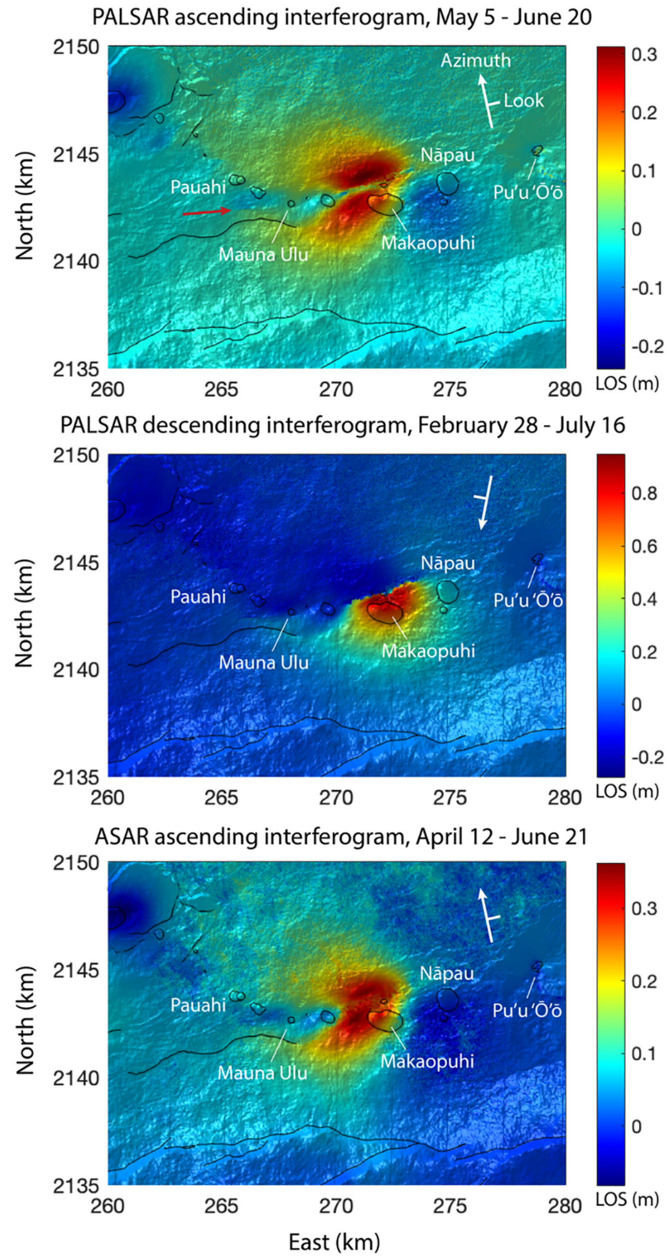

Fig. 3. Unwrapped interferograms and associated dates for this study. Red arrows indicate minor discontinuity corresponding to region of initial seismicity (See Fig. 1). (For interpretation of the references to color in this figure legend, the reader is referred to the web version of this article.)

3. Datasets and methods

3.1. Radar remote sensing: InSAR displacements and azimuth offsets

Two synthetic aperture radar (SAR) satellites were operating during the 2007 FD event: the Phased Array type L-band (wavelength ~ 23 cm) Synthetic Aperture Radar (PALSAR) aboard the first Advanced Land Observation Satellite (ALOS-1) and the C-band (wavelength ~ 6 cm) Advanced Synthetic Aperture Radar (ASAR) aboard the European Space Agency's Envisat land observation satellite (Table 1).

Interferometric synthetic aperture radar (InSAR) is a powerful geodetic technique to retrieve surface displacements (“deformation interferograms”) over hundreds of kilometers wide areas in the line-of-sight (LOS) direction with a (sub-)centimetric accuracy under favorable conditions (Massonnet and Feigl, 1998; Hanssen, 2001; Simons and Rosen, 2007). Three interferograms span the entire FD event without including the next intrusion of July 21 (Fig. 3). One interferogram was processed from a pair of ascending Envisat scenes and two others from ascending and descending ALOS-1 pairs (Table 2). All datasets were processed using software developed by GAMMA Remote Sensing (Wegmüller and Werner, 1997). The three interferograms were topographically corrected using a 4.5 m resolution LiDAR DEM, courtesy of HVO staff, to remove phase contributions due to elevation.

Because SAR satellites are near-polar orbiting (~N-S orbit tracks), InSAR data alone are unable to resolve N-S surface displacements. This inherent technique limitation can be overcome using cross correlation techniques. This method is referred to as pixel tracking, speckle tracking, or range/azimuth offsets. This approach has lower sensitivity that InSAR with an accuracy corresponding to ~1/10th of the original pixel size resolution (for ALOS-1, this corresponds to ~0.3 m) (Werner et al., 2005). However, an advantage of pixel tracking is that the calculated deformation measurements do not need to be unwrapped. Instead of using speckle- or pixel-tracking methods to retrieve the along-track component of displacement, Bechor and Zebker (2006) and Jung et al. (2011, 2014) proposed an alternative technique: Multiple

Table 1
Summary of main SAR datasets characteristics, as well as deformation interferograms and offset tacking pair used in inversions.

SAR acquisition date (MMDDYYYY)	Satellite	Orbit pass	Path, Frame, Beam (for ALOS-1)	Wavelength (cm)	Incidence angle (°)	
02282007	ALOS-1	Descending	601, 3230, FBD	23	39	
07162007	ALOS-1	Descending	601, 3230, FBS	23	39	
05052007	ALOS-1	Ascending	291, 370, FBD	23	39	
06202007	ALOS-1	Ascending	291, 370, FBD	23	39	
04122007	ASAR-Envisat	Ascending	136, 387	5.6	34 (IS4)	
06212007	ASAR-Envisat	Ascending	136, 387	5.6	34 (IS4)	
InSAR pair	Acquisition dates	Bperp (m)	Goldstein filter strength	Number of subsampled points		
ALOS-1 descending	02282007–07162007	252	0.4	948		
ALOS-1 ascending	05072007–06202007	324	0.4	908		
Envisat ascending	04122007–06212007	183	0.4	721		
Offset tracking pairs	Acquisition dates	Patch size	SNR	Correlation threshold		Number of subsampled points
ALOS-1 ascending	05072007–06202007	64 × 192	7	0.2		448

Aperture Interferometry (MAI). This consists in splitting the aperture normally used for a single differential interferogram into two separate interferograms using the forward and backward squinting SLCs (relative to the nominal squint angle for the standard SLC). These two interferograms can then in turn be differenced to produce a map of along-track displacements. They showed accuracies on the order of a few centimeters when the interferometric coherence was excellent. In areas of lower coherence, the phase difference-derived estimates were comparable to typical azimuth offsets estimates. Despite the increased accuracy of MAI in extracting along-track displacements relative to offset tracking (Jung et al., 2014), a disadvantage of the method is that the MAI interferogram must be unwrapped, like regular differential interferograms, which can introduce unwrapping errors. Another disadvantage is our case it that to obtain high coherence and thus robust MAI results, high multilooking factors must be used (Table S1 in the supplementary material), leading to a lower spatial resolution deformation product than obtained with conventional InSAR.

For the FD event, the azimuth direction for ascending scenes (Figs. 3 and 4) is more optimally aligned to observe the mainly NNW-SSE opening direction of the FD dike. After comparing the results obtained with MAI and the GAMMA intensity offset tracking algorithm (Werner et al., 2000, 2005) on the two available ascending SAR datasets (Fig. 4 and S1, S2, S3 in the supplementary material), we selected the azimuth offsets obtained from for the ascending ALOS scenes to use in our inversions because it was the dataset that was the most consistent with the offset recorded by the GPS stations (Fig. 4). Also, note that although range offsets are calculable using the same method, the predominately north-south deformation trend of the FD event means that the range offsets will be too small to be properly recorded and are thus not used in subsequent inversions. Search kernel dimensions influence the deformation field, with larger search windows tending to increase the accuracy of the obtained displacement field at a cost of increased computational load (Yun et al., 2007). Here, azimuth offsets were estimated by cross-correlating 64 × 192 pixel windows, with steps of 1 and 5 pixels in range and azimuth. A cross-correlation threshold of 0.2 was used to remove obvious outliers while retaining good coverage.

We reduce the number of sample points for all four selected deformation datasets (Table 1) through a circular subsampling technique following the approach of (Fukushima et al., 2005). A circular grid is defined for each dataset centered near the locus of the cumulative deformation at 2143242 N, 272401E in UTM zone 5 N. Each circular grid samples the dataset at 200 m intervals out to a 1 km radius; points beyond this radius are more sparsely sampled. Although the deformation signal is confined primarily to the region immediately surrounding the rift zone axis, we include subsampled points beyond the primary signal

Table 2
Summary of results for 50 joint inversions of the combined InSAR and offset tracking dataset, indicating the global lowest-misfit model obtained, the 95% confidence interval bounds, and the parameter limits imposed upon the inversion search stage. Free surface is at 830 m above sea level (average depth of all subsampled points).

Analytical inversion parameters					
Parameter	Lowest misfit	Lower 95%	Upper 95%	Min. Search Boundary	Max. Search Boundary
Opening (m)	2.3	1.67	2.42	0.1	10.0
Length (m)	2892	2015	5080	2000	6000
Width (m)	2404	2667	5583	2000	6000
Strike (deg)	73.1	67.0	73.5	60	110
Dip (deg)	83.3	73.2	92.8	60	110
Easting (UTM)	270,363	269,630	270,631	267,000	273,000
Northing (UTM)	2,142,850	2,141,827	2,143,190	2,140,500	2,143,000
Bottom depth (m, below free surface)	2420	2077	4923	2000	5000
Top depth (m, below free surface)	32.4				
Volume (m^3)	1.6e+07	0.9e+06	6.9 + 07	–	–
RMS (cm)	11.4				

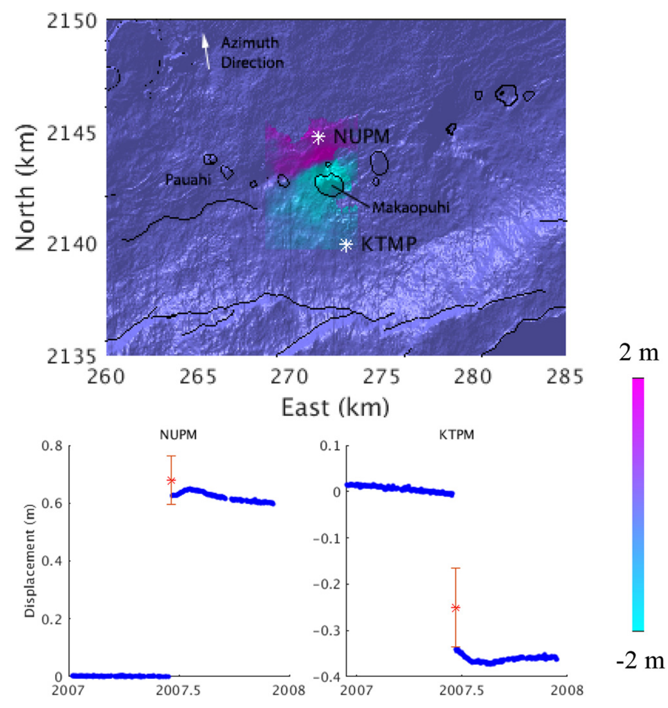

Fig. 4. Azimuth-direction offset field spanning the FD event with comparison to GPS daily displacement solutions at stations NUPM and KTPM of the Hawaiian Volcano Observatory permanent network (courtesy HVO). We find a standard deviation of 0.027 pixels for the final azimuth direction offset field. Given an azimuth pixel spacing of ~3.2 m for both PALSAR images, this yields an uncertainty estimate of 8.6 cm for our error bars.

for each of the three interferograms to ensure modeled far-field deformation remains negligible (Kintner et al., 2019). Note that we did not invert for the GNSS/GPS data for the following three reasons: 1/ the stations were far from the eruptive fissure and dike location; therefore, they would constrain very little the dike geometry and opening compared to near-field InSAR data; 2/ the weighting between a few GPS datapoints and hundreds/thousands of subsampled InSAR points is always a tricky and rather arbitrary step (e.g., (Simons et al., 2002; Sudhaus and Jonsson, 2009), and 3/ we were interested in the modeling of the entire event, not a dynamic dike propagation analysis in which the higher temporal resolution of GPS would be of extreme added value (i.e., (Segall et al., 2013).

3.2. Geodetic modeling: tested forward solutions

Models which have been obtained for past ERZ intrusions vary in geometry, ranging from rectangular dislocations (Owen et al., 2000; Conway et al., 2018) to two en-echelon dikes (Montgomery-Brown et al., 2010) or irregularly-distributed independent openings (Lundgren et al., 2013). We test a variety of forward models to assess the fit of several potential scenarios. First, a single Okada tensile dislocation (dike). Second, the following numerical models: 1) a single quadrangle exploring similar geometries as the Okada dislocations but allowing for discretized openings and quadrangular structures, 2) a branching system consisting of a single quadrangle connected to a pair of echelon segments which terminate below the primary discontinuity axis visible in the ALOS ascending interferograms, and finally, 3) a two-echelon model connecting a single quadrangle to the primary regions of cracked and steaming ground observed on June 18th, 2007, after the onset of eruptive activity (Fig. 1) (Tim Orr, Pers. Comm, 2020; Montgomery-Brown et al., 2010). Poisson's ratio and Young's modulus are set to 0.25 and 5 GPa, respectively (note that the latter only plays a role in the 3D-MBEM models).

3.2.1. Okada analytical solutions

To analyze the deformation field induced by dike intrusions, we have considered an oversimplified scenario of a uniformly-opening, tensile dislocation (Okada, 1985) embedded in an isotropic, homogeneous, elastic half space (Battaglia et al., 2013). The only published preferred model for the 2007 FD event includes two en-echelon dike segments ("2007 M-B" on Fig. 2) composed of rectangularly gridded, opening tensile Okada dislocations, and decollement slip modeled as similarly gridded, slipping Okada reverse fault calculations (Montgomery-Brown et al., 2010).

3.2.2. 3D-MBEM numerical solutions

Here, we also employ a three-dimensional Mixed Boundary Elements Method (3D-MBEM, (Cayol and Cornet, 1997)) which allows us to consider realistic topographies, any number and shapes of stress sources (massive or fracture), as well as their interactions (Fig. S4 in the supplementary material). The opening distribution is obtained through applying a uniform magma overpressure assuming all parts of the dike intrusion are hydraulically connected (Cayol and Cornet, 1997; Wauthier et al., 2012). This approach allows us to test whether or not the two echelon segments identified in (Montgomery-Brown et al., 2010) are fed by a single rooted dike as evidenced at other volcanoes like for instance Nyiragongo (Wauthier et al., 2012), Nyamulagira (Wauthier et al., 2013, 2015), and Piton de La Fournaise (Fukushima et al., 2010). The ability of 3D-MBEM to take into account stress interactions between multiple deformation sources additionally allows us to test the effect of a freely-slipping decollement plane on magma intrusions and vice-versa.

3.3. Non-linear inversions of surface displacements

The Neighbourhood Algorithm is a two-stage, iterative direct search method which seeks an ensemble of preferred model parameters through guided Monte Carlo sampling of parameter space (Sambridge, 1999a). The misfit of each forward model is defined as the covariance-weighted L_2 norm (χ^2) of the modeled and observed data u_m and u_o respectively for model m:

$$\chi^2(m) = (u_0 - u_m)^T C^{-1} (u_0 - u_m) \tag{1}$$

with covariance matrix C which can account for both the variance and spatial correlation of noise in data observations (Sambridge, 1999a; Fukushima et al., 2005). Here, we chose to assume no spatial noise correlation and thus *C* is diagonal (Kintner et al., 2019). We conduct inversions using 50 initial sample populations, followed by 10 additional models in each iteration distributed throughout the 10 lowest regions of the previous iteration. To compare our results with previous studies and offer a measure of misfit which is comparable between different datasets and more intuitive, we also calculate a root-mean-square (RMS) error in centimeters according to the formula:

$$RMS = 100 * \sqrt{\frac{(u_0 - u_m)^T (u_0 - u_m)}{N}} \tag{2}$$

for observed data points u_0, modeled data points u_m, and number of subsampled data points N (Fukushima et al., 2005).

The appraisal stage assesses all misfit values calculated during the search stage and constructs 1-D and 2-D PDFs with uncertainty estimates for each parameter using Monte Carlo integration along points which approximate the PDF in each Voronoi cell (Sambridge, 1999b; Fukushima et al., 2005). These PDFs represent the solution to the inversion problem and indicate which combinations of parameters lead to misfit-minimizing forward model regions. The robustness of the final PDF uncertainty estimates can be improved by combining the results of multiple search stages prior to the appraisal stage to ensure a thorough search of parameter space (Kintner et al., 2019). For inversion of simple analytical dislocation solutions, we execute 50 independent inversion sequences and combine their PDF results to obtain a thorough search and characterization of parameter space. This method creates approximately 150,000 data points sampling parameter space for the combined dataset.

3.4. Static Coulomb stress change analysis

The Coulomb stress change ΔS acting upon a plane is defined as:

$$\Delta S = \Delta\tau + \mu' \Delta\sigma \tag{3}$$

for shear stress change $\Delta\tau$, normal stress change $\Delta\sigma$, and effective fault coefficient μ' (Toda et al., 2011). This calculation quantifies the changes in shear and normal stress resulting from magma overpressure or volume change in magma reservoirs or pathways ("sources" of stress), on potential fault planes ("receivers" of stress) (Oppenheimer et al., 1988; Harris and Simpson, 1992). By the given convention, regions of positive Coulomb stress change indicate slip is encouraged along the receiver fault planes, while negative values indicate a dominance of friction and normal stress which inhibits slip along these planes. We use the United States Geological Survey (USGS) software package Coulomb 3.3 (Toda et al., 2011) for calculation of three-dimensional stress fields within an elastic homogeneous half-space based on the equations of Okada, 1992 (Okada, 1992). We assume changes in value of the effective frictional coefficient μ' do not substantially influence the final Coulomb stress change field and set it to 0.4 for all calculations (Wauthier et al., 2012). For calculations of Coulomb stress changes along the proposed decollement geometry, we use a Young's Modulus of 70 GPa corresponding to the ~8 km depth of the decollement (Conway et al., 2018).

4. Preferred geodetic models

4.1. Preferred Okada model

Using the Neighbourhood Algorithm, we obtain 2D PDF solutions and lowest-misfit forward models for a rectangular Okada dislocation

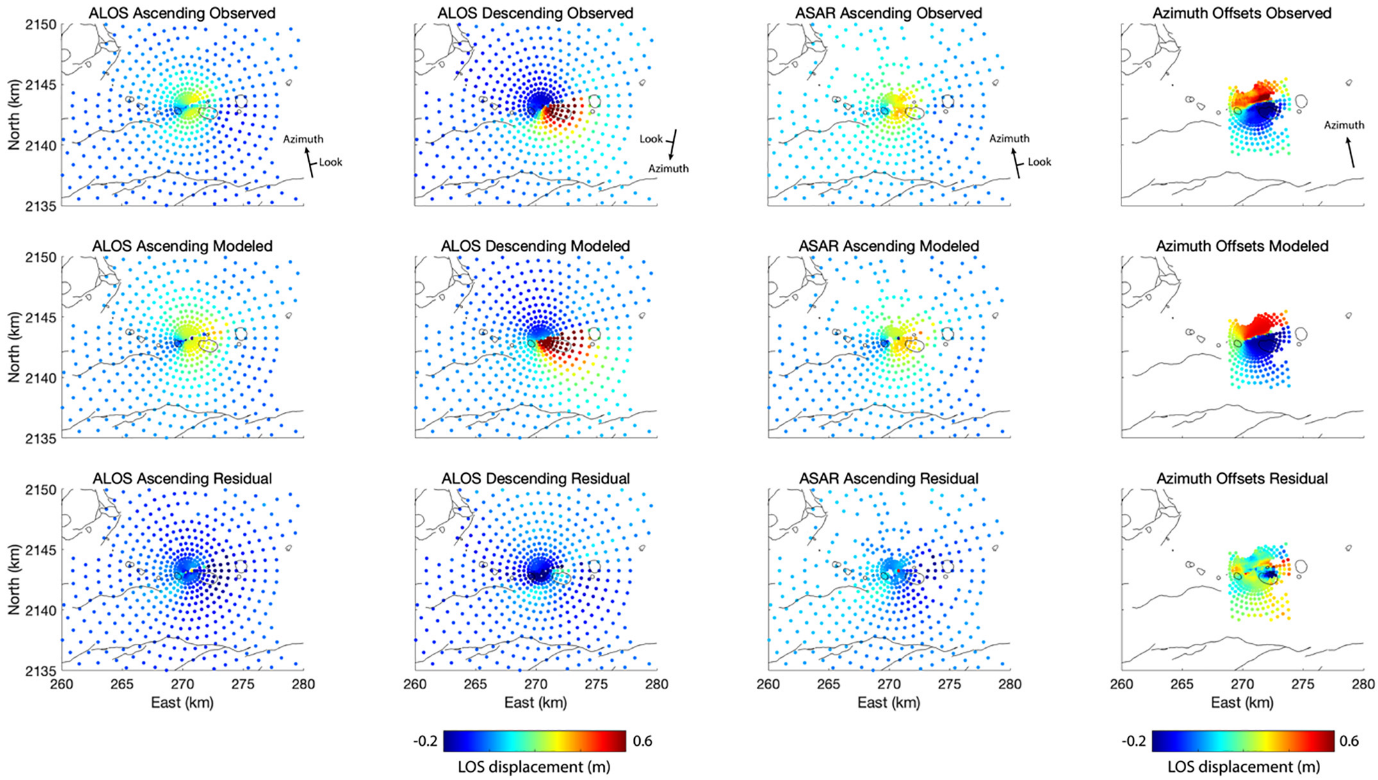

Fig. 5. Observed, modeled, and residual subsampled datapoints derived from three InSAR interferograms and the azimuth offset tracking field for the lowest-misfit analytical model (Table 2). The summit region has been omitted for all three interferograms as the source of this deformation is not modeled, and data points within a region of low coherence due to effusion from Pu'u 'Ō'ō during the InSAR acquisition period is also removed. The full color extend of the residuals (third row) is shown in Fig. S6 in the supplementary material.

for a joint inversion of all four datasets combined. The width and depth parameters are both poorly constrained in the inversion 1D PDF solutions, with a trade-off relationship evident between them in the corresponding 2D PDFs (Fig. S5 in the supplementary material). The overall lowest misfit model (RMS = 11.4 cm) for all datasets opens 2.3 m, strikes 73 degrees while dipping sub-vertically at 83.3 degrees, and extends approximately 2.9 km to the ENE and 2.4 km downdip (Table 2, Fig. 5). The preferred dike extends between 32.4 and 2420 m below the reference surface, which corresponds to between 798 above sea level and 1590 m below sea level if we assign the mean elevation of our data points (830 m above-sea level) as the reference surface (Chaussard and Amelung, 2012) (Fig. 6).

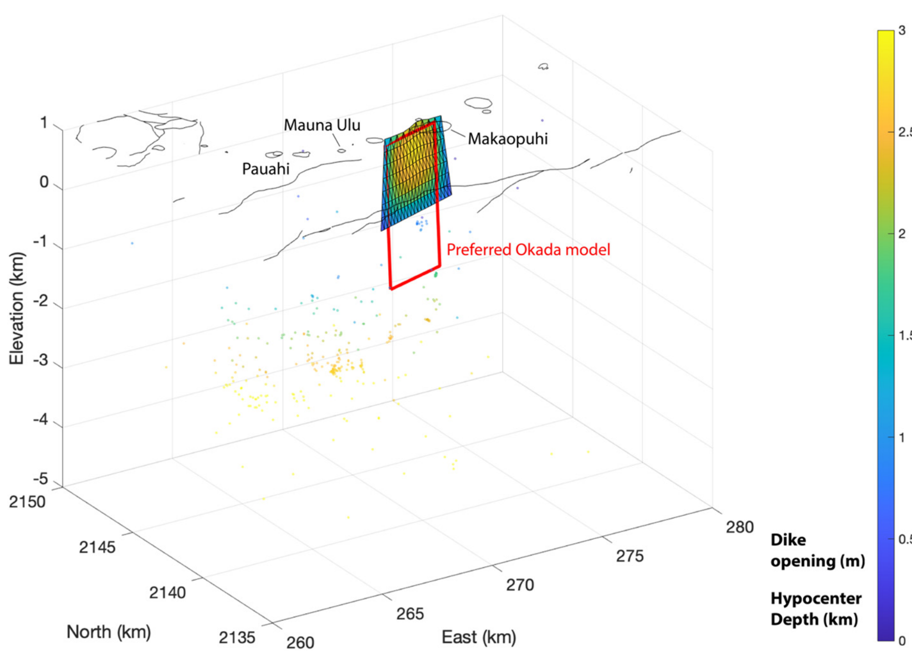

Fig. 6. Comparison of lowest-misfit non-breaching 3D-MBEM model (Table 3) and analytical model for joint inversion of all datasets combined (in red, Table 2). Depth values for the analytical model have been normalized to the surface reference of the local topography using a surface reference of the half space of 830 m (average depth of all subsampled points). Earthquakes spanning June 17–19, 2007 are also indicated (Matoza et al., 2013). Opening for the Okada tensile dislocation is uniform and equals to 2.3 m.

Table 3
Lowest-misfit model parameters obtained during search stage inversions for each of the four proposed 3D-MBEM dike models shown in Fig. 7. Note that dip is fixed to 83.3° (dip corresponding to the lowest misfit Okada). RMS is calculated for data vectors comprised of interferogram datapoints with offset tracking data included.

3D-MBEM models					
Structure	OP (MPa)	Bot Elev. (m)	Main quadrangular part top depth (m)	RMS (cm)	Volume (m^3)
Non-breaching	4.3	−550	33	10.5	1.06e+07
Single breach	3.0	−690	32	10.5	1.08e+07
Non-breaching, free decollement	3.4	−1140	30	10.4	1.14e+07
Single breach, free decollement	3.7	−660	26	10.4	1.11e+07

4.2. Preferred 3D-MBEM model

The lowest-misfit 3D-MBEM solution for a single quadrangle with no connection to the ground surface (Table 3, first row) is based on the location derived from analysis of the lowest misfit analytical model in such a way that the southernmost corner defining the dike location is set equal to the coordinates of the lowest-misfit tensile dislocation model obtained during joint inversion of all datasets (Table 2). Note that inverting that corner as well does not lead to major changes in our results and dike extent/orientation (Fig. 7B and D). Additionally, we fixed the dip to that of the lowest Okada solution (dip = 83.3°).

We performed a joint inversion of all four datasets for the following five free parameters: dike overpressure (OP), dip, bottom and top elevation, and the top length parameter which allows the geometry of the quadrangle to deviate from a rectangle (Fig. S4 in the supplementary material). The lowest misfit was obtained for a dike originating at ~550 m below sea level and terminating ~33 m below the topography (Table 3, first row). The length of the dike at its bottom is ~1.3 times its top length, with an overpressure of ~4.3 MPa corresponding to an average opening of ~1.9 m and a maximum opening of 2.8 m. This model provides an RMS of 10.5 cm (Fig. 8), which is insignificantly lower than the preferred analytical model for a joint inversion of all datasets of 10.4 cm. Considering one (Fig. 7B, Table 3) or two (Fig. S10 in the supplementary material) surface breaches connected to the eruptive fissure and other cracked areas do not improve the fit significantly either.

We repeated the same inversion sequence which yielded our optimum breaching and non-breaching MBEM models with the inclusion of a decollement plane striking approximately 63 degrees east of north and dipping toward the northwest at 15 degrees (Montgomery-Brown, et al., 2009 & 2010). We set its depth to lie between 6 km and 9 km based on previous studies of focal mechanism solutions, earthquake hypocenter location, and seismic tomography for Kīlauea's south flank (Wright and Klein, 2014; Montgomery-Brown et al., 2013; Lin et al., 2015; Judson et al., 2018). The decollement geometry is included as a free-slipping fracture with no imposed traction. While including a decollement changes the lowest misfit bottom/top ratio and overpressure/openings slightly (Fig. 7C and D), the improvement in fit and RMS is negligible (Table 3 and Fig. S8 in the supplementary material).

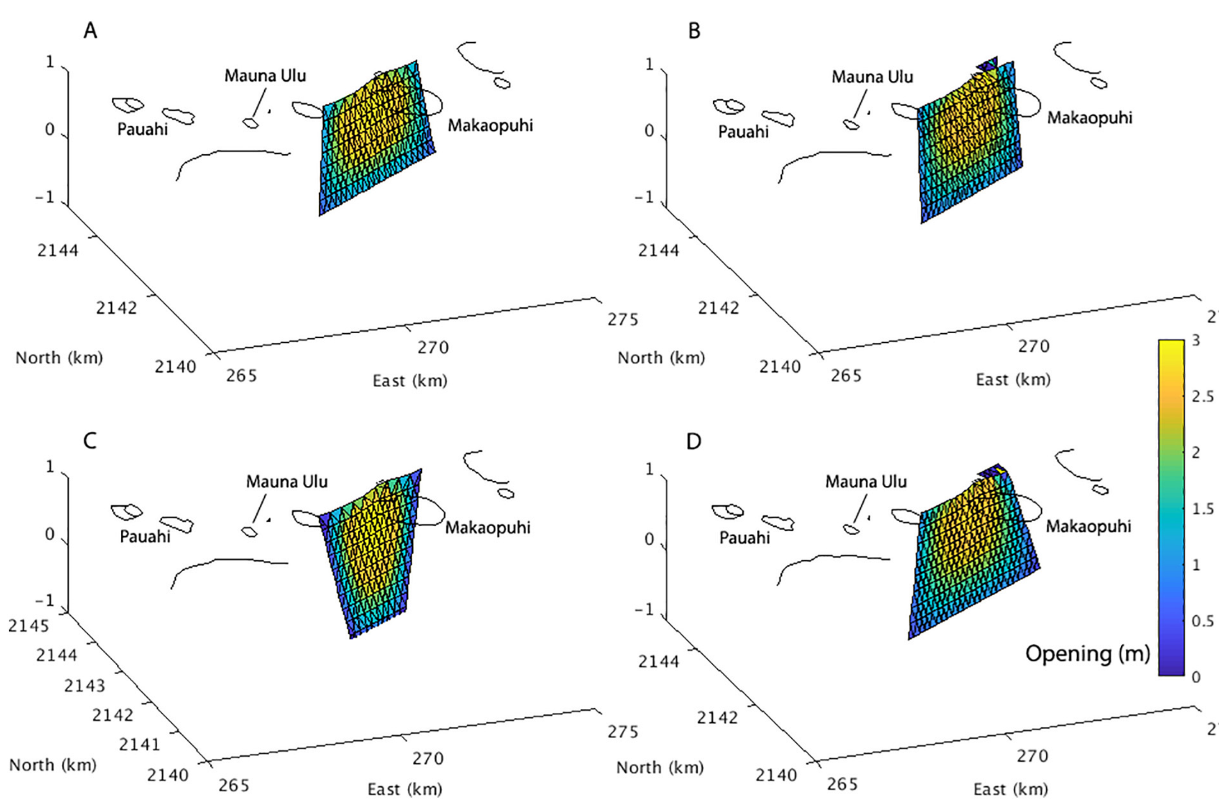

Fig. 7. Preferred dike geometries and openings using 3D-MBEM. A) Non-breaching dike without decollement influence. B) Single-breach dike without decollement influence. The lowest-misfit, single-breach solution is obtained with four additional inverted parameters: two which allow movement of the corner point defining location, and two which define the points at which a breaching segment connects to the primary quadrangle. Dip is held constant at 83.3°. C) Non-breaching dike, freely slipping decollement surface. D) Single breach dike, freely slipping decollement. Note that the introduction of a variable corner point does not significantly influence the preferred orientation of the dike (Fig. 7B and D), with the optimum location of this and other 3D-MBEM quadrangles coinciding well with the position of the lowest-misfit analytical model (Fig. 6).

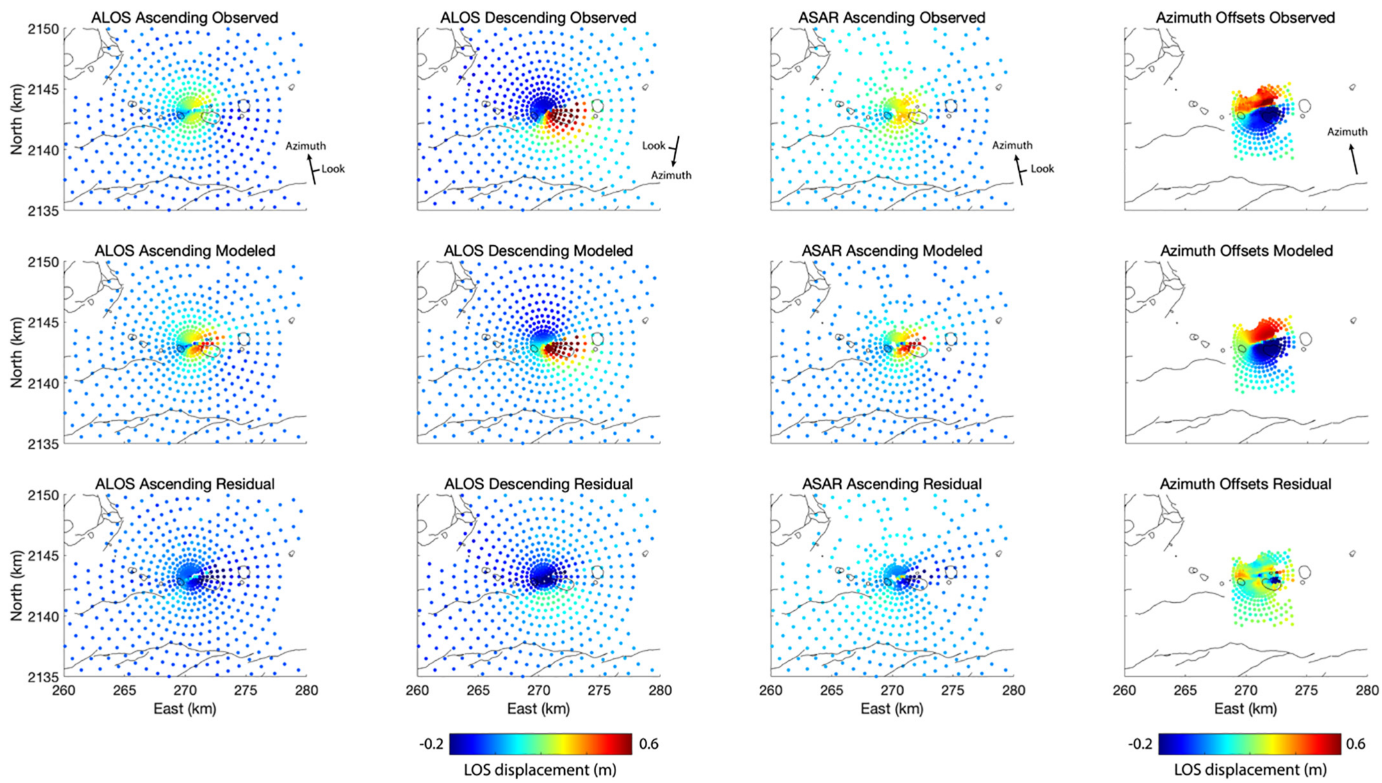

Fig. 8. Observed, modeled, and residual subsampled datapoints derived from three InSAR interferograms and the azimuth offset tracking field for the lowest-misfit single-breach model without freely slipping decollement (Table 3). The summit region has been omitted for all three interferograms as the source of this deformation is not modeled, and data points within a region of low coherence due to effusion from Puʻu ʻŌʻō during the InSAR acquisition period is also removed. The full color extend of the residuals (third row) is shown in Fig. S7 in the supplementary material. Note that Fig. S8 in the supplementary material shows the lowest misfit 3D-MBEM models with decollement.

5. Discussion

5.1. Comparison with previous studies

The only other published model for the 2007 FD event includes two en-echelon dike segments and decollement slip (Montgomery-Brown et al., 2010). The parameters for these models were determined via a two-step inversion process consisting of an initial non-linear Monte Carlo inversion to determine the optimum geometry of a single uniformly-opening tensile dislocation, with openings subsequently determined via a non-negative least-squares algorithm (Montgomery-Brown et al., 2010). Total volume for both dikes was 1.65e+7 m^3, with the larger eastern dike contributing 95.2% of this overall volume, which matches extremely well our preferred Okada dike volume of 1.6e+7m^3. The volumes obtained in our 3D-MBEM models range between 1.06e+7 and 1.14e+7 m^3 (Table 3), with slightly larger volumes found when including the decollement. Using Okada solutions seems to overestimate the dike volume, as previously noted in (Fukushima et al., 2005).

The data vector used to calculate misfit during the inversion stages contained 1172 points obtained from GPS, tilt, and InSAR measurements (Montgomery-Brown et al., 2010). The RMS error for the displacements created by this model when measured against our two combined datasets are presented in Table 4. Since the slipping patches representing the decollement can be modeled independently from the dike tensile opening patches, we include RMS values calculated for dike-only models, and for dike models with decollement slip included. The RMS errors calculated for the previous en-echelon system using our datasets are internally comparable, and the results (Table 4) indicate that adding a decollement plane is not justified by the SAR datasets to decrease the misfit. Since the main focus here is on the dike intrusion, we do not take this part of the study any further. In the future, however, including other data sets could improve the ability to resolve deformation of the decollement that occurs mainly in the along-track (N-S) direction with very little vertical deformation (Chen, 2014).

5.2. Preferred models: implications for intrusion geometry

All models uniformly indicate preference for an extremely shallow dike top (Tables 2 and 3) within ~30 m of the surface. This shallow emplacement is consistent with the extensive cracking and steaming of the ground combined with minor lava effusion northeast of Makaopuhi and with previous diking events along the ERZ (Montgomery-Brown et al., 2010; Lundgren et al., 2013; Owens el al., 2018). The more flexible geometry of the 3D-MBEM models does not improve the fit significantly compared to simpler tensile Okada dislocations. The lowest-misfit non-breaching 3D-MBEM and Okada models are similar in geometry and location to previous ERZ intrusions (Fig. 2), particularly the February 1993 passive event (Conway et al., 2018). 3D-MBEM models tend to have shallower bottom depths (ranging between 550 and 1140 below sea level, see Table 3) than the preferred Okada, which reaches a depth of 1590 below sea level after correction for the reference surface at 830 m above sea level. Earlier comparison of 3D-MBEM results to analytical dislocation solutions noted a similar tendency of the Okada-type

Table 4
RMS error values calculated for the models derived by (Montgomery-Brown et al., 2010) using our data vectors comprised of interferogram datapoints with offset tracking data included.

(Montgomery-Brown et al., 2010) en-echelon model		
Dataset	Model Type	RMS (cm)
InSAR + Offset tracking	Dike only	20.7
InSAR + Offset tracking	Dike + Decollement	20.7

solutions to overestimate the depth of the intrusion (Fukushima et al., 2005). While our dike models are all shallower than typical values of ~3 km for origin depths of ERZ intrusions (Poland et al., 2014), magma-induced seismicity observed during the initial onset of the intrusive event exhibits hypocenters between 1 km and 3 km depth (Fig. 1).

5.3. Magma source for the 2007 FD intrusion

Uniformly higher misfits obtained for 3D-MBEM models with multiple, hydraulically-connected surficial sections indicate that a single magma pulse was likely not responsible for the two events observed on June 17 modeled by two distinct echelons in (Montgomery-Brown et al., 2010). Thus, one possibility is that the observed deformation signal results from two independent magma pulses from the summit or ERZ reservoirs on June 17 which rose separately from magma moving through the shallow ERZ conduit (Montgomery-Brown et al., 2010). Alternatively, a second possibility is that a normal fault within the Koa'e fault zone directly west of the observed deformation slipped in response to stress changes from magma emplacement at the eastern location. Given that the observed InSAR discontinuity coincides with an apparent fault scarp showing ~7 m of displacement between its foot and hanging walls, this second possibility seems more likely. Coulomb stress changes for optimum normal faults as a result of the FD intrusion emplacement indicate favorable stress changes for normal fault slip (Fig. 9). However, the extent of cracked ground observed near Mauna Ulu and Chain of Craters Road (Fig. 1) combined with the onset of clustered seismicity in the region beginning early morning of June 17 indicate movement of magma near the surface. This suggests that, although slip along a steeply dipping normal fault may be responsible for the location and strike of this observed western discontinuity and local ground deformation, two distinct pulses of magma are likely still required to account for ground cracking as well as the temporal and spatial distinction of the seismicity pattern.

5.4. Impact of decollement slip

Models which include a free-slipping decollement do not exhibit significantly lower RMS errors compared to dike-only models, regardless of whether the modeling technique is analytical or 3D-MBEM (Tables 3 and 4). However, inversions for breaching and non-breaching 3D-MBEM models obtain considerably different values for quadrangle depth and bottom/top ratios when a decollement is included, suggesting a trade-off relationship between concurrent fault slip and dike emplacement which facilitates dike opening at depth and allows the emplacement of dikes under lower magma overpressure or increased quadrangle bottom depth and bigger volume (Fig. 7 and Table 3). A similar behavior was noted by (Lundgren et al., 2013) for a model of the March 2011 Kamoamoa fissure eruption, in which feedback between decollement slip and dike opening resulted in model trade-offs between these parameters below 4 km. The inclusion of modeled slip along the decollement fault also does not provide a significant improvement to the modeled displacements at GPS stations NUPM and KTPM. Based on these results, we conclude that decollement

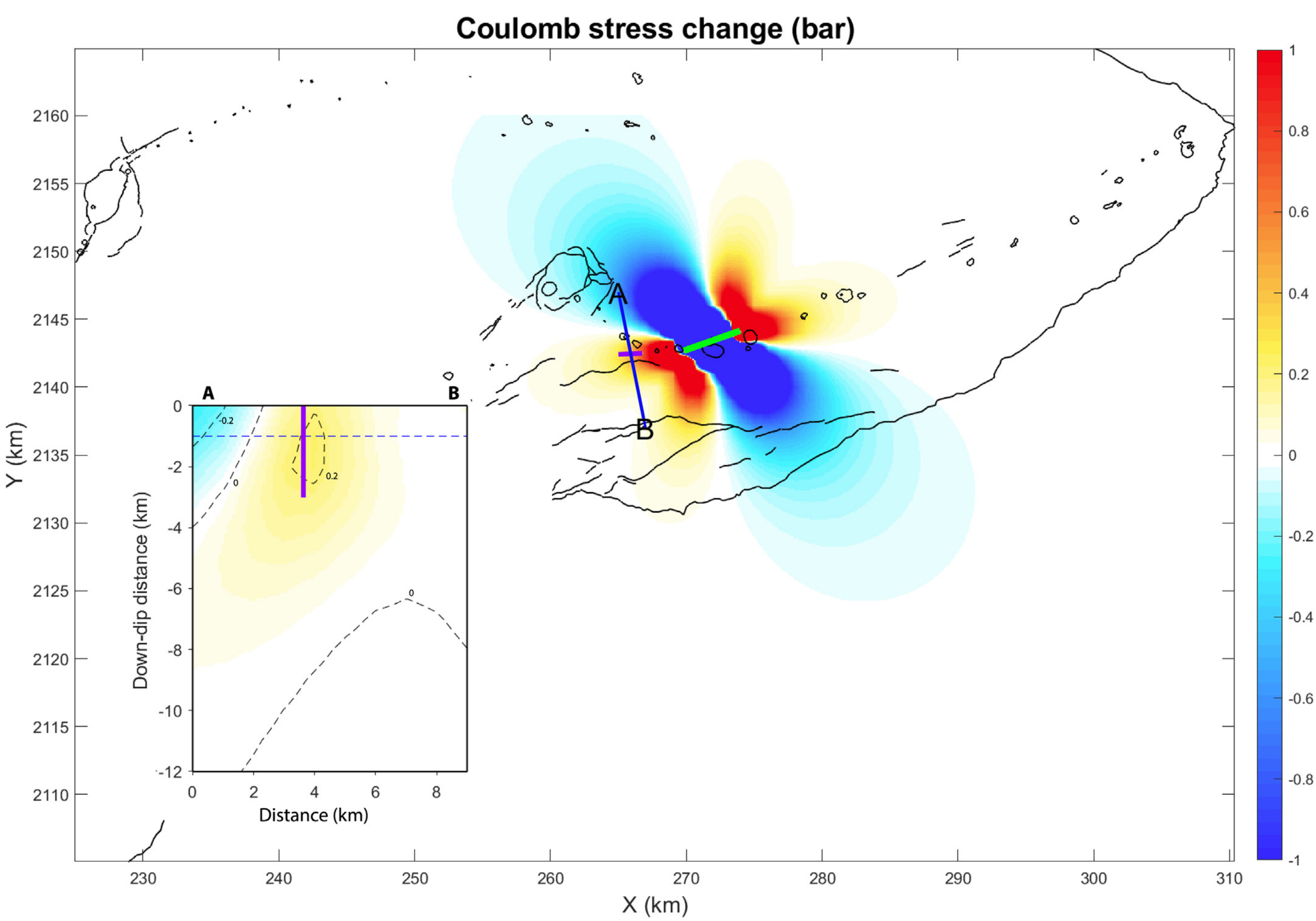

Fig. 9. Coulomb stress changes calculated for optimal normal faults (purple trace) based on the lowest-misfit 3D-MBEM non-breaching model (green trace) at 1 km depth. Cross section contour interval is 0.2 bars. (For interpretation of the references to color in this figure legend, the reader is referred to the web version of this article.)

slip may generally influence the geometry of an ERZ intrusion if the slip is concurrent with the dike emplacement, but decollement slip itself will not produce a notable deformation signal in the vicinity of the ERZ. Furthermore, given the SSE onset well after the intrusive activity of the FD event had begun (Brooks, 2008; Montgomery-Brown et al., 2010 & 2011), there seems to be little possibility of the SSE influencing the intrusion geometry directly. This confirms the prior classification of the intrusion as an active event, stemming directly from pressurization of magma storage at Kilauea's summit without significant effect of a dynamic, co-emplacement stress regime (Brooks et al., 2008; Montgomery-Brown et al., 2010).

5.5. Stress interactions: implications for triggering of the SSEs

We compare the stress changes acting on generic faults parallel to the decollement geometry for two magmatic sources of stress: the non-breaching FD event 3D-MBEM intrusion geometry derived from our inversion sequences (Table 3, first row), and the optimal deep rift opening 3D-MBEM model obtained by Conway et al. (2018) for the 1993–1997 period. Although this latter model was obtained for an earlier period of Kīlauea's eruptive history, the role of deep rift zone dilation as a driving factor for decollement slip has been well-documented (e.g., Cayol et al., 2000; Poland et al., 2012; Wright and Klein, 2014). Furthermore, linear seaward slip rates documented by GPS stations KAEP, GOPM, and PGF3 from 2000 to 2010 indicate steady deep rift opening and flank slip rates throughout the entire period, with increasing magma supply recorded during the 2003–2007 summit inflationary period being accommodated within the shallow rift zone and pressurized storage within the south caldera reservoir at the summit (Poland et al., 2014; Wauthier et al., 2016; Wauthier et al., 2019). We therefore consider the model of (Conway et al., 2018) to be generally representative of continued deep rift zone expansion preceding the 2007 FD event and useful for comparative analysis with the stress change field derived from the 2007 FD intrusion.

Investigation of hourly GPS records during the event have suggested onset of slow slip 15–20 h after the intrusion (Brooks et al., 2008) with slip progressing east to west along the decollement plane (Montgomery-Brown et al., 2011). This was also observed during the 2018 magnitude 6.9 earthquake in which the rupture front propagated southwest along the decollement from an initial central hypocenter (Liu et al., 2018). This timing seems to favor the triggering of the 2007 SSE event by the 2007 FD dike intrusion. However, when considering the FD intrusion as source of stress (Fig. 10), Coulomb stress changes are negative onshore at the depths of the decollement (Fig. 10 A – B). The seismicity which began ~20 h after the onset of the intrusion (Fig. 1) falls within the regime of negative Coulomb stress change, indicating

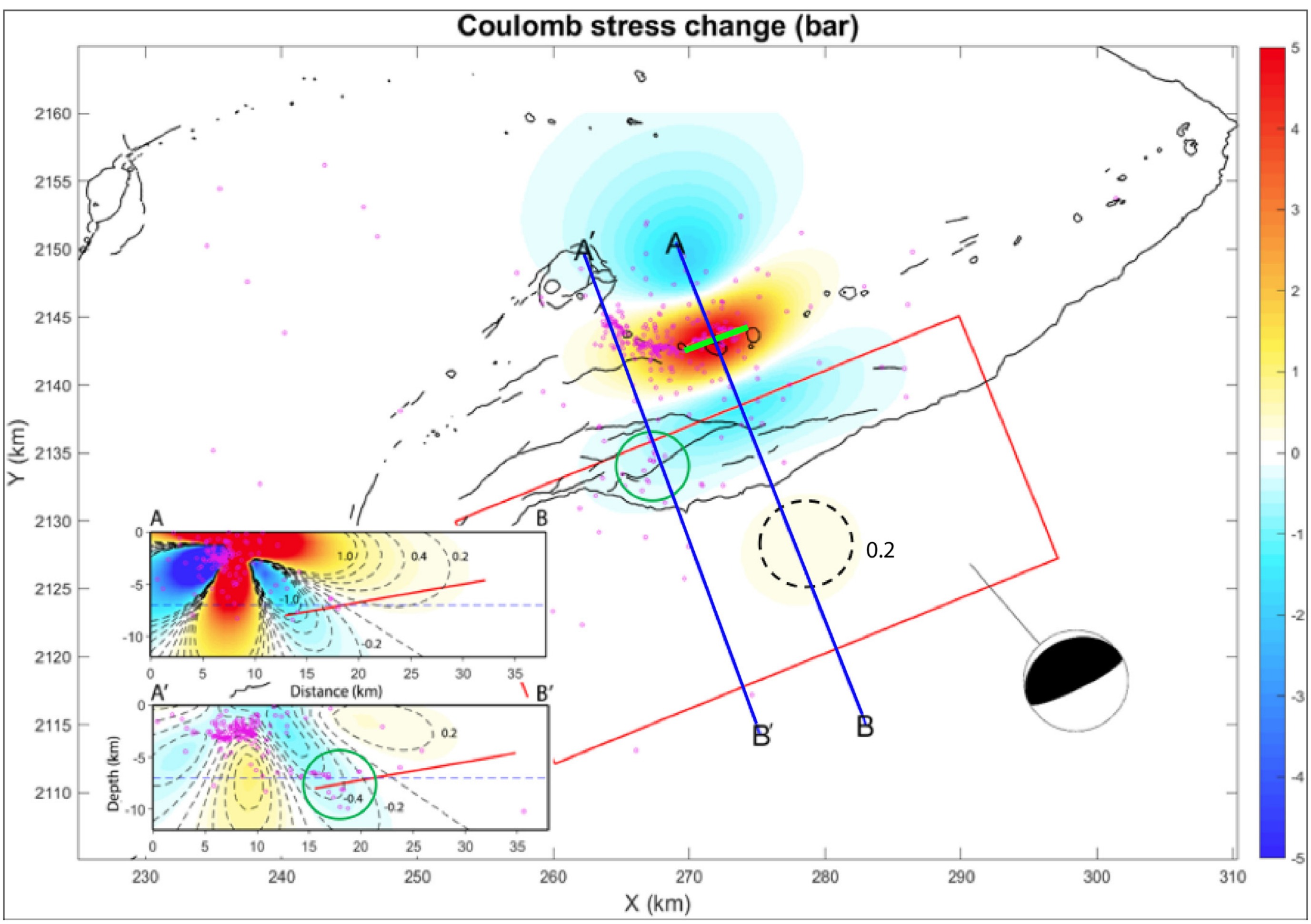

Fig. 10. Coulomb stress changes calculated at 7 km depth and in cross section (insets) for generic receiver faults of same geometry as the proposed decollement fault plane (red). Stresses are derived from 260 tensile opening dislocations approximating the lowest-misfit non-breaching 3D-MBEM model geometry obtained via inversion (green trace). Young's modulus is 70 GPa, Poisson's ratio is 0.25, frictional coefficient is 0.4. Violet circles represent migrated earthquake hypocenters spanning June 17 through June 20, 2007. Large green circles indicate hypocenters which were previously determined to be shallow-angle thrust faults located on the decollement plane during the 2007 FD SSE (Syracuse et al., 2010). Proposed decollement plane strikes 243 degrees and dips 15 degrees to the NW with a rake of 90. Cross section contour interval is 0.2 bars; 0.2 bar threshold indicated in map view. (For interpretation of the references to color in this figure legend, the reader is referred to the web version of this article.)

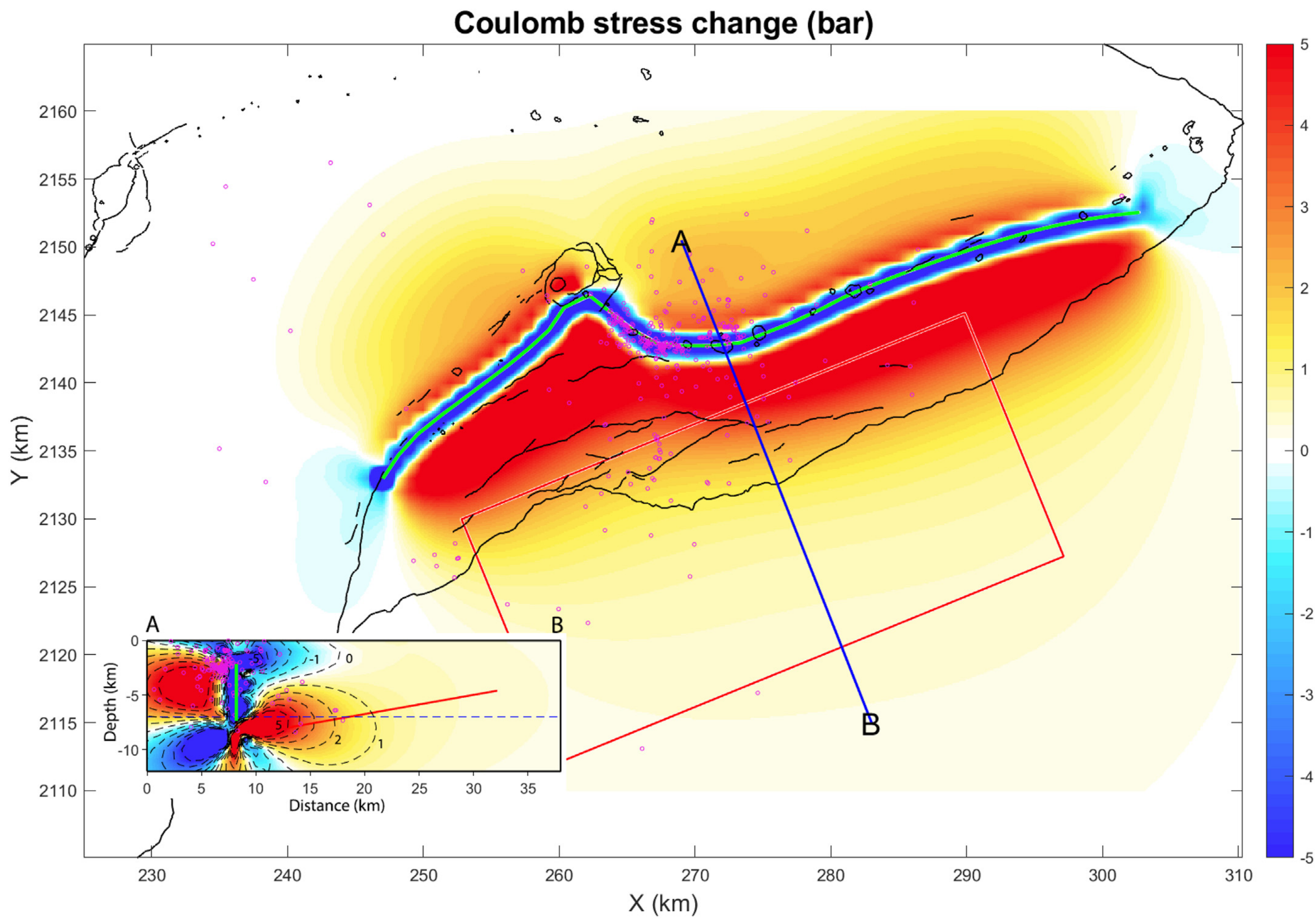

Fig. 11. Coulomb stress changes for same receiver fault geometry and elastic parameters as in Fig. 10. Cross section contour interval is 1 bar. Stresses are derived from 94 tensile opening dislocations representing cumulative deep rift zone opening over the period 1993–1997 using a 3D-MBEM model (green trace) from (Conway et al., 2018). (For interpretation of the references to color in this figure legend, the reader is referred to the web version of this article.)

inhibition to slip. Small positive Coulomb stress changes are only observed along the updip portion of the decollement perpendicular to the intrusion further offshore, ~15 km south of the ERZ (Fig. 10). Focal mechanisms obtained previously for decollement seismic events preceding and during the 2007 FD intrusion yielded slightly different decollement geometries than those modeled here, although we test the effect of these geometric variations on the resulting Coulomb stress change field and find no significant difference in the distribution of stress changes, although magnitudes vary slightly with geometry (Supplementary information Fig. S11 – S13 in the supplementary material) (Syracuse et al., 2010; Liu et al., 2018). This means that geometric variations along the decollement itself will not affect our interpretations, and as seen with similar solutions derived for the 2018 intrusive event, intrusions along the ERZ will likely manifest Coulomb stress changes of similar location in subsequent events (Kundu et al., 2020) with potentially higher magnitudes with larger dike opening such as the four meters modeled in 2018 (Neal et al., 2019).

When considering the optimal model for deep rift opening of (Conway et al., 2018) obtained for the period of 1993–1997 (average opening of ~0.55 m) as source of stress, positive Coulomb stress changes indicating facilitated slip are observed along the entire length of the proposed decollement plane (Fig. 11). The seismicity cluster which coincided with the slow slip event following the FD intrusion is included in this region. Therefore, we suggest that the slow-slip event following the FD intrusion was not triggered by the shallow FD intrusion but instead that the timing and triggering of SSEs at Kilauea is primarily related to deep rift dilation processes.

6. Conclusions

Most of the deformation observed during the 2007 FD event can be satisfactorily fit by a single intrusive structure located beneath Makaopuhi (Fig. 12). We find that more complex numerical 3D-MBEM

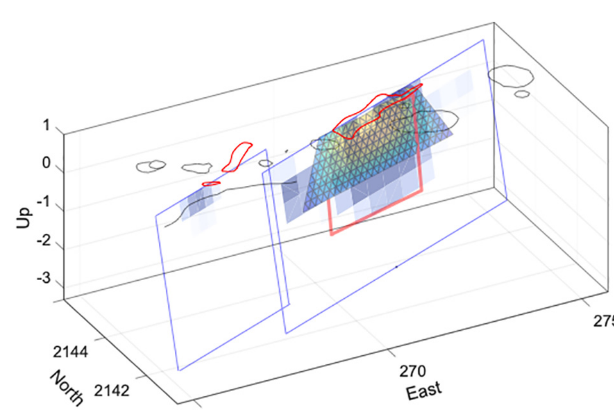

Fig. 12. 3D view of the en-echelon model (blue rectangles) of (Montgomery-Brown et al., 2010), as well as the overall preferred single Okada model (red rectangle, this study) and the preferred 3D-MBEM model (opening distribution as shown in Fig. 6 and 7A, this study). (For interpretation of the references to color in this figure legend, the reader is referred to the web version of this article.)

models allowed to breach the surface and/or considering a free-slipping decollement plane result in negligible improvements to model fit. The deformation field is poorly fit by single dike features with hydraulically connected superficial breach segments, suggesting two independent pulses originating from the ERZ shallow conduit with possible slip on a normal fault along the Koa'e system. Evidence from Coulomb stress changes suggest that deep rift zones dilation processes modulate the timing and triggering of slow-slip events at Kilauea.

Author contributions

This work originates from Jeffrey Leeburn MSc thesis at the Pennsylvania State University, supervised by C.Wauthier. InSAR, Geodetic, and stress modeling were performed by J. Leeburn and C. Wauthier. J. Gonzalez-Santana processed MAI results. All authors read and contributed to improving the manuscript.

Declaration of Competing Interest

The authors declare that they have no known competing financial interests or personal relationships that could have appeared to influence the work reported in this paper.

Acknowledgements

This work was funded by the Pennsylvania State University as part of Jeffrey Leeburn MSc Thesis. The authors would like to thank Peter LaFemina and Charles Ammon at the Pennsylvania State University for constructive comments that helped improve an earlier version of this manuscript. The authors acknowledge continuous support from the HVO USGS staff. Wauthier is supported by National Science Foundation (NSF) CAREER (EAR 1945417) grant:" Career: Numerical Modeling of Volcanic Flank Instability Processes"). Finally, the authors would like to thank Paul Lundgren, Francisco Delgado and one anonymous reviewer and the editor Alessandro Aiuppa for their helpful and constructive comments and review.

Appendix A. Supplementary data

Supplementary data to this article can be found online at https://doi.org/10.1016/j.jvolgeores.2021.107425.

References

Anderson, K.R., Poland, M.P., 2016. Bayesian Estimation of Magma Supply, Storage, and Eruption Rates Using a Multiphysical Volcano Model: Kīlauea Volcano, 2000–2012.

Anderson, K.R., Poland, M.P., Johnson, J.H., Miklius, A., 2015. Episodic Deflation–Inflation Events at Kīlauea Volcano and Implications for the Shallow Magma System. John Wiley & Sons, Inc., Hoboken, NJ, pp. 229–250 https://doi.org/10.1002/9781118872079.ch11.

Bagnardi, M., Poland, M.P., Carbone, D., Baker, S., Battaglia, M., Amelung, F., 2014. Gravity changes and deformation at kīlauea volcano, hawaii, associated with summit eruptive activity, 2009–2012. J. Geophys. Res. Solid Earth 119 (9), 7288–7305. https://doi.org/10.1002/2014JB011506.

Baker, S., Amelung, F., 2012. Top-down inflation and deflation at the summit of kīlauea volcano, Hawaiʻi observed with InSAR. J. Geophys. Res. Solid Earth 117 (B12). https://doi.org/10.1029/2011JB009123 n/a.

Battaglia, M., Cervelli, P.F., Murray, J.R., 2013. DMODELS: a MATLAB software package for modeling crustal deformation near active faults and volcanic centers. J. Volcanol. Geotherm. Res. 254, 1–4. https://doi.org/10.1016/j.jvolgeores.2012.12.018.

Bechor, N.B., Zebker, H.A., 2006. Measuring two-dimensional movements using a single InSAR pair. Geophys. Res. Lett. 33 (16).

Brooks, B.A., Foster, J.H., Bevis, M., Frazer, L.N., Wolfe, C.J., Behn, M., 2006. Periodic slow earthquakes on the flank of kīlauea volcano, Hawaiʻi. Earth Planet. Sci. Lett. 246 (3), 207–216. https://doi.org/10.1016/j.epsl.2006.03.035.

Brooks, B.A., Foster, J., Sandwell, D., Wolfe, C.J., Okubo, P., Poland, M., Myer, D., 2008. Magmatically triggered slow slip at Kilauea Volcano. Hawaii: Science 321. https://doi.org/10.1126/science.1159007 1177–1177.

Cayol, V., Cornet, F.H., 1997. 3D mixed boundary elements for elastostatic deformation field analysis. Int. J. Rock Mech. Min. Sci. 34 (2), 275–287. https://doi.org/10.1016/S0148-9062(96)00035-6.

Cayol, V., Dieterich, J.H., Okamura, A.T., Miklius, A., 2000. High Magma Storage Rates Before the 1983 Eruption of Kilauea. Hawaii: Science (New York, N.Y.) 288, 2343–2346. https://doi.org/10.1126/science.288.5475.2343.

Cervelli, P., Miklius, Asta, 2003. The Shallow Magmatic System of Kilauea Volcano. US Geological Survey Professional Paper. 1676.

Cervelli, P., Segall, P., Amelung, F., Garbeil, H., Meertens, C., Owen, S., Miklius, A., Lisowski, M., 2002. The 12 September 1999 Upper East Rift Zone dike intrusion at Kilauea Volcano, Hawaii. J. Geophys. Res. 107, 1–13. https://doi.org/10.1029/2001JB000602.

Chaussard, E., Amelung, F., 2012. Precursory inflation of shallow magma reservoirs at west Sunda volcanoes detected by InSAR. Geophys. Res. Lett. 39. https://doi.org/10.1029/2012GL053817.

Chen, J., 2014. Insar Time Series Analysis of Subtle Transient Crustal Deformation Signals Associated With the 2010 Slow Slip Event At Kilauea, Hawaii. 127 p http://purl.stanford.edu/jt439bk7846 (accessed August 2021).

Conway, S., Wauthier, C., Fukushima, Y., Poland, M., 2018. A retrospective look at the February 1993 east rift zone intrusion at Kilauea volcano, Hawaii. J. Volcanol. Geotherm. Res. 358, 241–251. https://doi.org/10.1016/j.jvolgeores.2018.05.017.

Delaney, P.T., Fiske, R.S., Miklius, A., Okamura, A.T., Sako, M.K., 1990. Deep magma body beneath the summit and rift zones of Kilauea volcano, Hawaii. Science 247 (4948), 1311–1316. https://doi.org/10.1126/science.247.4948.1311.

Denlinger, R.P., Okubo, P., 1995. Structure of the mobile south flank of kilauea volcano, hawaii. J. Geophys. Res. Solid Earth 100 (B12), 24499–24507. https://doi.org/10.1029/95JB01479.

Fukushima, Y., Cayol, V., Durand, P., 2005. Finding realistic dike models from interferometric synthetic aperture radar data: the February 2000 eruption at Piton de la Fournaise. J. Geophys. Res. 110, B03206. https://doi.org/10.1029/2004JB003268.

Fukushima, Y., Cayol, V., Durand, P., Massonnet, D., 2010. Evolution of magma conduits during the 1998-2000 eruptions of Piton de la Fournaise volcano, Réunion Island. J. Geophys. Res. Solid Earth 115, 1–21. https://doi.org/10.1029/2009JB007023.

Garcia, M.O., 2003. A petrologic perspective of kilauea volcano's summit magma reservoir. J. Petrol. 44 (12), 2313–2339. https://doi.org/10.1093/petrology/egg079.

Global Volcanism Program [GVP], 2009. Report on Kīlauea (United States). In: Wunderman, R. (Ed.), Bulletin of the Global Volcanism Network. 34. Smithsonian Institution, p. 3. https://doi.org/10.5479/si.GVP.BGVN200903-332010.

Hanssen, R.F., 2001. Radar Interferometry: Data Interpretation and Error Analysis.

Harris, R.A., Simpson, R.W., 1992. Changes in static stress on southern california faults after the 1992 landers earthquake. Nature 360 (6401), 251–254. https://doi.org/10.1038/360251a0.

Heliker, C., Mattox, T.N., 2003. The first two decades of the Pu' u 'Ō'ō-Kūpaianaha eruption: chronology and selected bibliography. US Geol. Surv. Prof. Pap. 1–20.

Hill, D.P., 1969. Crustal structure of the island of Hawaii from seismic refraction measurements. Bull. Seismol. Soc. Am. 59, 101–130.

Hill, D.P., Zucca, J.J., 1987. Geophysical constraints on the structure of Kilauea and Mauna Loa volcanoes and some implications for seismomagmatic processes. US Geol. Surv. Prof. Pap. 1350, 903–917.

Judson, J., Thelen, W.A., Greenfield, T., White, R.S., 2018. Focused seismicity triggered by flank instability on Kīlauea's Southwest Rift Zone. J. Volcanol. Geotherm. Res. 353, 95–101. https://doi.org/10.1016/j.jvolgeores.2018.01.016.

Jung, H.S., Lu, Z., Won, J.S., Poland, M.P., Miklius, A., 2011. Mapping three-dimensional surface deformation by combining multiple-aperture interferometry and conventional interferometry: application to the June 2007 eruption of Kilauea volcano, Hawaii. IEEE Geosci. Remote Sens. Lett. 8 (1), 34–38. https://doi.org/10.1109/LGRS.2010.2051793.

Jung, H.S., Lee, W.J., Zhang, L., 2014. Theoretical accuracy of along-track displacement measurements from multiple-aperture interferometry (MAI). Sensors 14 (9), 17703–17724.

Kintner, J.A., Wauthier, C., Ammon, C.J., 2019. InSAR and seismic analyses of the 2014–15 earthquake sequence near Bushkan, Iran: shallow faulting in the core of an anticline fold. Geophys. J. Int. 217 (2), 1011–1023. https://doi.org/10.1093/gji/ggz06.

Kundu, B., Yadav, R.K., Bürgmann, R., Wang, K., Panda, D., Gahalaut, V.K., 2020. Triggering relationships between magmatic and faulting processes in the may 2018 eruptive sequence at kīlauea volcano, hawaii. Geophys. J. Int. 222 (1), 461–473. https://doi.org/10.1093/gji/ggaa178.

Lin, G., Shearer, P.M., Amelung, F., Okubo, P.G., 2015. Seismic tomography of compressional wave attenuation structure for Kīlauea Volcano, Hawaiʻi. J. Geophys. Res. Solid Earth 120, 2510–2524. https://doi.org/10.1002/2014JB011594.

Liu, C., Lay, T., Xiong, X., 2018. Rupture in the 4 May 2018 MW 6.9 earthquake seaward of the Kilauea east rift zone fissure eruption in Hawaii. Geophys. Res. Lett. 45 (18), 9508–9515. https://doi.org/10.1029/2018GL079349.

Lundgren, P., Poland, M., Miklius, A., Orr, T., Yun, S.-H., Fielding, E., Liu, Z., Tanaka, A., Szeliga, W., Hensley, S., Owen, S., 2013. Evolution of dike opening during the March 2011 Kamoamoa fissure eruption, Kīlauea Volcano, Hawai`i. J. Geophys. Res. Solid Earth 118, 897–914. https://doi.org/10.1002/jgrb.50108.

Lundgren, P.R., Bagnardi, M., Dietterich, H., 2019. Topographic changes during the 2018 Kīlauea eruption from single-pass airborne InSAR. Geophys. Res. Lett. 46, 9554–9562. https://doi.org/10.1029/2019GL083501.

Macdonald, G.A., Abbott, A.T., Peterson, F.L., 1983. Volcanoes in the Sea: The Geology of Hawaii. 2nd ed. University of Hawaii Press, Honolulu.

Matoza, R.S., Shearer, P.M., Lin, G., Wolfe, C.J., Okubo, P.G., 2013. Systematic relocation of seismicity on Hawaii Island from 1992 to 2009 using waveform cross correlation and cluster analysis. J. Geophys. Res. Solid Earth.

Massonnet, D., Feigl, K.L., 1998. Radar interferometry and its application to changes in the earth's surface. Rev. Geophys. 36, 441–500.

Montgomery-Brown, E.K., Miklius, A., 2021. Periodic dike intrusions at Kilauea volcano, Hawaiʻi. Geology 49, 397–401. https://doi.org/10.1130/G47970.1.

Montgomery-Brown, E.K., Sinnett, D.K., Poland, M., Segall, P., Orr, T., Zebker, H., Miklius, A., 2010. Geodetic evidence for en echelon dike emplacement and concurrent slow slip during the june 2007 intrusion and eruption at kīlauea volcano, hawaii. J. Geophys. Res. Solid Earth 115 (B7). https://doi.org/10.1029/2009JB006658 n/a.

Montgomery-Brown, E.K., Sinnett, D.K., Larson, K.M., Poland, M.P., Segall, P., Miklius, A., 2011. Spatiotemporal evolution of dike opening and décollement slip at kīlauea volcano, hawai'i. J. Geophys. Res. Solid Earth 116 (B3). https://doi.org/10.1029/2010JB007762 n/a.

Montgomery-Brown, E.K., Thurber, C.H., Wolfe, C.J., Okubo, P., 2013. Slow slip and tremor search at kilauea volcano, hawaii: Kilauea Slow Slip and Tremor Search. Geochem. Geophys. Geosyst. 14 (2), 367–384. https://doi.org/10.1002/ggge.20044.

Myer, D., Sandwell, D., Brooks, B., Foster, J., Shimada, M., 2008. Inflation along Kīlauea's Southwest Rift Zone in 2006. J. Volcanol. Geotherm. Res. 177 (2), 418–424. https://doi.org/10.1016/j.jvolgeores.2008.06.006.

Neal, C.A., Brantley, S.R., Antolik, L., Babb, J.L., Burgess, M., Calles, K., ... Damby, D., 2019. The 2018 rift eruption and summit collapse of Kīlauea volcano. Science (New York, N.Y.) 363 (6425), 367–374. https://doi.org/10.1126/science.aav7046.

Okada, Yoshimitsu, 1985. Surface deformation due to shear and tensile faults in a half-space. Int. J. Rock Mech. Min. Sci. Geomech. Abstr. 23 (4), 128. https://doi.org/10.1016/0148-9062(86)90674-1.

Okada, Yoshimitsu, 1992. Internal deformation due to shear and tensile faults in a half-space. Bull. Seismol. Soc. Am. 82 (2), 1018–1040. https://doi.org/10.1785/BSSA0820021018.

Oppenheimer, D.H., Reasenberg, P.A., Simpson, R.W., 1988. Fault plane solutions for the 1984 morgan hill, california, earthquake sequence: evidence for the state of stress on the calaveras fault. J. Geophys. Res. Solid Earth 93 (B8), 9007–9026. https://doi.org/10.1029/JB093iB08p09007.

Owen, S., Segall, P., Lisowski, M., Miklius, A., Murray, M., Bevis, M., Foster, J., 2000. January 30, 1997 eruptive event on kilauea volcano, hawaii, as monitored by continuous GPS. Geophys. Res. Lett. 27 (17), 2757–2760. https://doi.org/10.1029/1999GL008454.

Pietruszka, A.J., Garcia, M.O., 1999. The size and shape of kilauea volcano's summit magma storage reservoir: a geochemical probe. Earth Planet. Sci. Lett. 167 (3), 311–320. https://doi.org/10.1016/S0012-821X(99)00036-9.

Poland, M., Miklius, A., Orr, T., Sutton, J., Thornber, C., Wilson, D., 2008. New episodes of volcanism at Kīlauea Volcano, Hawaii. Eos Trans. AGU 89 (5), 37–38. https://doi.org/10.1029/2008EO050001.

Poland, M.P., Takahashi, T.J., Landowski, C.M., 2014. Characteristics of Hawaiian volcanoes. U.S. Geol. Surv. Prof. Pap. 1801. https://doi.org/10.3133/pp1801 428 p.

Poland, B.M.P., Miklius, A., Montgomery-Brown, E.K., Poland, M.P., Miklius, A., Montgomery-Brown, E.K, 2014. Magma Supply, Storage, and Transport at Shield-Stage Hawaiian Volcanoes. U.S. Geol. Surv. Prof. Pap., v. Not Publis, 1–52 https://doi.org/10.3133/pp1801.

Sambridge, M., 1999a. Geophysical inversion with a neighbourhood algorithm—I. Searching a parameter space. Geophys. J. Int. 138, 479–494.

Sambridge, M., 1999b. Geophysical inversion with a neighbourhood algorithm—II. appraising the ensemble. Geophys. J. Int. 138 (3), 727–746. https://doi.org/10.1046/j.1365-246x.1999.00900.x.

Segall, P., Llenos, A.L., Yun, S.H., Bradley, A.M., Syracuse, E.M., 2013. Time-dependent dike propagation from joint inversion of seismicity and deformation data. J. Geophys. Res. Solid Earth 118, 5785–5804. https://doi.org/10.1002/2013JB010251.

Simons, M., Rosen, P.A., 2007. Author ' s Personal Copy 3. 12 Interferometric Synthetic Aperture Radar Geodesy: Aperture. 3, pp. 391–446.. http://ieeexplore.ieee.org/xpls/abs_all.jsp?arnumber=1024984.

Simons, M., Fialko, Y., Rivera, L., 2002. Coseismic Deformation from the 1999 Mw 7.1 Hector Mine, California, Earthquake as Inferred from InSAR and GPS Observations. Bull. Seismol. Soc. Am. 92, 1390–1402. https://doi.org/10.1785/0120000933.

Sudhaus, H., Jonsson, S., 2009. Improved source modelling through combined use of InSAR and GPS under consideration of correlated data errors: Application to the June 2000 Kleifarvatn earthquake, Iceland. Geophys. J. Int. 176, 389–404. https://doi.org/10.1111/j.1365-246X.2008.03989.x.

Swanson, D.A., Fiske, R.S., Thornber, C.R., Poland, M.P., 2018. Dikes in the Koa 'e Fault System, and the Koa 'e–East Rift Zone Structural Grain at Kīlauea Volcano, Hawai 'i. 538. Geological Society of America Special Publication, pp. 247–274.

Syracuse, E.M., Thurber, C.H., Wolfe, C.J., Okubo, P.G., Foster, J.H., Brooks, B.A., 2010. High-resolution locations of triggered earthquakes and tomographic imaging of kilauea volcano's south flank. J. Geophys. Res. Solid Earth 115 (B10). https://doi.org/10.1029/2010JB007554 n/a.

Toda, S., Stein, R.S., Sevilgen, V., Lin, J., 2011. Coulomb 3.3 Graphic-rich deformation and stress-change software for earthquake, tectonic, and volcano research and teaching—user guide. U.S. Geological Survey Open-File Report 2011–1060 63 p https://pubs.usgs.gov/of/2011/1060/.

Wauthier, C., Cayol, V., Kervyn, F., d'Oreye, N., 2012. Magma sources involved in the 2002 Nyiragongo eruption, as inferred from an InSAR analysis. J. Geophys. Res. Solid Earth 117 (B5). https://doi.org/10.1029/2011JB008257 B05411-n/a.

Wauthier, C., Roman, D.C., Poland, M.P., 2013. Moderate-magnitude earthquakes induced by magma reservoir inflation at Kīlauea volcano, Hawai'i: M4+ Earthquakes Induced by Magma Supply. Geophys. Res. Lett. 40 (20), 5366–5370. https://doi.org/10.1002/2013GL058082.

Wauthier, C., Cayol, V., Smets, B., d'Oreye, N., Kervyn, F., 2015. Magma pathways and their interactions inferred from InSAR and stress modeling at Nyamulagira volcano, D.R. Congo. Remote Sens. 7, 15179–15202. https://doi.org/10.3390/rs71115179.

Wauthier, C., Roman, D.C., Poland, M.P., 2016. Joint analysis of geodetic and earthquake fault-plane solution data to constrain magmatic sources: a case study from Ki'lauea volcano. Earth Planet. Sci. Lett. 455, 38. https://doi.org/10.1016/j.epsl.2016.09.011.

Wauthier, C., Roman, D.C., Poland, M.P., 2019. Modulation of seismic activity in Kīlauea's upper east rift zone (Hawai'i) by summit pressurization. Geology 47 (9), 820–824. https://doi.org/10.1130/G46000.1.

Wegmüller, U., Werner, C., 1997. Gamma SAR processor and interferometry software. Eur. Space Agency Spec. Publ. 1687–1692 (ESA SP).

Werner, C., Wegmuller, U., Strozzi, T., Wiesmann, A., 2000. GAMMA SAR and Interferometric Processing Software. European Space Agency, (Special Publication) ESA SP.

Werner, C., Wegmüller, U., Strozzi, T., Wiesmann, A., 2005. Precision Estimation Of Local Offsets Between Pairs of SAR SLCs and Detected SAR Images. pp. 25–29.

Wright, T.L., Klein, F.W., 2014. Two hundred years of magma transport and storage at Kīlauea Volcano, Hawai'i, 1790–2008. U.S. Geol. Surv. Prof. Pap. 1806, 1790–2008. https://doi.org/10.3133/pp1806.

Yun, S., Zebker, H., Segall, P., Hooper, A., Poland, M., 2007. Interferogram formation in the presence of complex and large deformation. Geophys. Res. Lett. 34 (12). https://doi.org/10.1029/2007GL029745 L12305-n/a.